Discovery of giant magnetofossils within and outside of the Palaeocene-Eocene Thermal Maximum in the North Atlantic

Pengfei Xue[1], Liao Chang[1,2,*], Zhaowen Pei[1], Richard J. Harrison[3]

1. Laboratory of Orogenic Belts and Crustal Evolution, School of Earth and Space Sciences, Peking University, Beijing 100871, P. R. China
2. Laboratory for Marine Geology, Qingdao National Laboratory for Marine Science and Technology, Qingdao 266071, P. R. China
3. Department of Earth Sciences, University of Cambridge, Cambridge, CB2 3EQ, UK

Giant magnetofossils have exceptionally large grain sizes and peculiar morphologies compared to conventional biogenic magnetite nanoparticles. The origin of these unusual magnetic crystals is a mystery because there are no known modern analogues. Giant magnetofossils have so far been identified in marine sediments deposited during past warming periods, leading to the assumption that these fossils were uniquely tied to ancient hyperthermal events. Here we describe the occurrence of abundant giant magnetofossils within North Atlantic pelagic sediments from International Ocean Discovery Program (IODP) Sites U1403 and U1409 at distinct palaeodepths not only during the Palaeocene-Eocene Thermal Maximum (PETM; ~56 Ma) intervals but also far before (>700 ky earlier than the PEB, Palaeocene-Eocene boundary) and after (>300 ky later than the PEB) the PETM, and in a sample of ~70 Ma age. Our results indicate that giant biogenic magnetite crystals were not uniquely produced during ancient hyperthermal events. Magnetic domain states of giant magnetite particles are investigated using dimensional analysis and micromagnetic simulations. Morphological, compositional, and crystallographic data point towards a potential biogenic origin of those unusual crystals.

1. Introduction

The Palaeocene-Eocene Thermal Maximum (PETM, ~56 Ma) is the most pronounced global warming event in the Cenozoic, characterized by a negative carbon isotope excursion (CIE) ranging from -2‰ to -4‰ and a temperature increase of more than 5 °C globally in less than 10 ky (McInerney and Wing, 2011; Zachos et al., 2008). The duration of the PETM is ~200–300 ky, which generally contains the CIE (~60–120 ky) and recovery phases (~80–120 ky) (McInerney and Wing, 2011). The CIE phase is further subdivided into CIE onset (<~20 ky) and CIE body intervals, although the CIE onset is absent in some pelagic cores because of widespread carbonate dissolution during the PETM (McInerney and Wing, 2011). Geological records of the PETM event provide potential insight into current and future global warming caused by anthropogenic greenhouse gas emissions (Tierney et al., 2020). A rapid evolution of marine ecosystems has been documented widely at the PETM onset, including the most severe benthic foraminiferal extinction over the past 90 Ma (Thomas, 2003, 2007; Alegret et al., 2021), geographic migration and body-size increase of planktonic foraminifera (Thomas, 1996; Petrizzo, 2007), and a burst in abundance and geographic range of heterotrophic dinoflagellates (Sluijs et al., 2007). A great disturbance in diversity, distribution and body sizes of marine organisms across the PETM may have been affected by high-temperature, low-oxygen conditions, severe corrosive seawater, altered productivity, or a combination of these (Thomas, 2007). Warming-induced environmental perturbation led to severe biotic effects on marine ecosystems, while unique biomarkers can be used to trace palaeoenvironmental changes across hyperthermal events.

The mysterious giant magnetofossils were firstly defined using scanning and transmission electron microscopy in the North Atlantic CIE body sediments from several near-shore boreholes at Ancora (ODP Leg 174AX), New Jersey (Schumann et al., 2008). Three novel crystal morphologies were identified: spearhead, spindle, and needle (Schumann et al., 2008). Another novel morphology of

giant bullet-shaped crystals together with other morphologies were discovered across the PETM in the Southern Ocean near Antarctica and during the Middle Eocene Climatic Optimum (MECO, ~40 Ma) in the western equatorial Indian Ocean, demonstrating their widespread occurrence in the geological record (Chang et al., 2012). Giant magnetofossils were identified in pelagic sediments not only during the PETM but also very shortly before and after the PETM on the Antarctic margin (Chang et al., 2012). Only giant needles were found within the PETM CIE peak in the Walvis Ridge, South Atlantic (Chang et al., 2018). Subsequent studies of CIE onset and body clay sediments in the North Atlantic attempted to estimate the concentration of giant magnetofossils (Wang et al., 2015; Wagner et al., 2021a, b) and detect in-situ giant needles (Wagner et al., 2021a, b), in addition to studying their morphologies. These techniques (Wang et al., 2015; Wagner et al., 2021a, b) may be applied to investigate the spatial occurrence of giant magnetofossils within sediments in their bulk state across past global warming intervals.

Unlike conventional magnetofossils, no modern organisms have yet been found that can produce magnetite crystals similar to giant magnetofossils. To date, giant magnetofossils have been discovered during or very closely tied to hyperthermal events (PETM, MECO), leading to a hypothesis that giant magnetofossil are uniquely linked to past global warmings (Fig. 1a) (Schumann et al., 2008; Kopp et al., 2009; Chang et al., 2012, 2018; Wang et al., 2015; Wagner et al., 2021a, b). These few studies limit an assessment of the spatial and temporal distribution of giant magnetofossils in the geological record. Solid evidence for the biogenic origin of giant magnetite crystals has yet been identified, although oxygen isotope measurements of a spearhead-like particle strongly support a biogenic origin forming during low-temperature crystallization rather than high-temperature igneous and metamorphic processes (Schumann et al., 2008). Conditions for giant biogenic magnetite formation is also not well known, although it is speculated that expanded suboxic zones during warming periods enhanced the diversification and proliferation of organisms that biomineralize biogenic magnetite (Schumann et al.,

2008; Kopp et al., 2009; Chang et al., 2012; Wagner et al., 2021b).

Here we carry out detailed scanning electron microscope (SEM) and transmission electron microscope (TEM) observations to search for giant magnetofossils within North Atlantic pelagic marine sediments from the International Ocean Discovery Program (IODP) Sites U1409 and U1403 covering the PETM intervals (Figs. 1, 2 and Table 1). High-resolution SEM and TEM characterization of giant magnetofossil crystals and statistical analysis of morphological data shed new light on the possible origin and mineralization of giant magnetite crystals and their link to ancient hyperthermal events. Crystal dimensions and micromagnetic simulations are performed to investigate domain states of these giant magnetite crystals.

2. Materials and methods

2.1. Samples

The studied pelagic marine sediment samples are from the Southeast Newfoundland Ridge (IODP Site U1409, ~2913 m palaeodepth) and the J-Anomaly Ridge (IODP Site U1403, ~4374 m palaeodepth) sediment drifts, North Atlantic (Fig. 1b). Carbon isotopic composition ($\delta^{13}C$) of bulk carbonate and benthic foraminifera both show an abrupt decrease followed by a gradual recovery at Site U1409 (Fig. 2a), characterizing the CIE body at 180.075–180.14 m composite depth (mcd, ~6.5 cm thick) and the main recovery interval at 179.9–180.075 mcd (17.5 cm thick), respectively (Penman et al., 2016). Sediments deposited during the CIE body are claystone, while sediments within the main recovery stage are a heterogeneous mixture of siliceous claystone and chert (Norris et al., 2012; Penman et al., 2016). Bulk $\delta^{13}C_{org}$ (organic carbon) record from the lower-abyssal Site U1403 reveals a negative CIE body from 200.7 to 201.5 mcd (80 cm thick), although the precise position of the CIE onset is uncertain (Penman et al., 2016) (Fig. 2b). Sediments from Site U1403 within the CIE body are clay with radiolarians, and the carbonate-rich sediments with nannofossil are featured during the CIE recovery

between 198.9 and 200.7 mcd (180 cm thick) (Norris et al., 2012; Penman et al., 2016). The age model for the PETM intervals at Sites U1409 and U1403 is derived from Penman et al. (2016) (Table 1). Because the sedimentation rate at Site U1409 is low and the position of the CIE onset at Site U1403 is uncertain (Fig. 2), the PETM intervals in this study are mainly characterized by the CIE body (75 ky) and recovery phases (125 ky) (Penman et al., 2016). Wet samples (~5 cm^3) were collected from the working half of cores stored at the IODP Bremen Core Repository.

2.2. Magnetic measurements

~Half wet sediments from different PETM stages at Sites U1409 and U1403 were freeze-dried, packed with capsules, and weighted for magnetic analyses. Isothermal remanent magnetization (IRM) acquisition curves and first-order reversal curve (FORC; Roberts et al., 2000) were measured with a Princeton Micromag vibrating sample magnetometer (Model 3900) at the Institute of Geophysics, China Earthquake Administration (IGCEA) in Beijing. Each IRM acquisition curve containing 80 data points was obtained in logarithmic steps up to 1 T maximum field, which was decomposed into different coercivity spectra using the MAX UnMix application (Maxbauer et al., 2016). 120 FORCs were made with a 1 T maximum field with an averaging times of 250 ms, with B_c ranging from 0 to 100 mT and B_u ranging from -50 to 50 mT. FORC data were processed with the VARIFORC protocol (Egli, 2013) using the FORCinel version 3.06 (Harrison and Feinberg, 2008).

2.3. TEM and SEM observations

Magnetic mineral extracts were obtained following the method of Chang et al. (2012) to prepare samples for TEM and SEM observations. First, ~2 cm^3 wet samples were dispersed in ~100 ml of pure water in a glass beaker for ~15 min in an ultrasonic bath. A rare-earth magnet placed into a plastic bag was dipped into the sediment solution and stirred for ~3 min to gather magnetic extracts on the plastic bag surface. After placing this plastic bag into a larger one and removing the rare-earth magnet, magnetic extracts were collected in the large plastic bag. This process was repeated until magnetic

extracts could barely be obtained from the sediment solution. The rest of the magnetic extracts attached to the plastic bag surface were washed with a small amount of pure water. Second, the solution with magnetic extracts was transferred into a 5 ml centrifuge tube filled with pure water using a pipette. A rare-earth magnet was placed next to the centrifuge tube and positioned ~0.5 cm higher than the bottom of the tube. After ~2 hours, non-magnetic materials deposited at the tube bottom were gently removed with a pipette, and magnetic materials trapped on the tube wall were collected. The separation for magnetic and non-magnetic materials was repeated three times to increase the concentration of magnetic minerals in the extracts.

To prepare TEM samples, magnetic materials with a small amount of pure water were first transferred into a small container. A TEM grid with the carbon side facing down was placed on the solution surface. A rare-earth magnet was suspended over the grid ~1 cm for ~5 min. Bright-field (BF) TEM imaging, selected area electron diffraction (SAED), energy dispersive spectra (EDS), and high-resolution transmission electron microscopy (HRTEM) imaging were carried out using a JEOL JEM-2100 TEM operated at 200 kV at the Institute of Geology and Geophysics, Chinese Academy of Sciences (IGGCAS) in Beijing.

To prepare SEM samples, the pipette containing magnetic materials with a small amount of pure water was suspended over a silicon wafer ~0.5 cm. Then a rare-earth magnet was placed next to the pipette for gathering magnetic minerals. After removing the rare-earth magnet, ~3–5 drops of the solution with magnetic mineral were dropped onto the silicon wafer dropwise. Samples were air-dried for ~8 hours at room temperature, and not coated with carbon before SEM observations due to the good electrical conductivity of silicon wafers. High-resolution secondary electron (SE) images were acquired at 15 kV with a working distance of ~6 mm. EDS were taken at 15 kV with a working distance of ~10 mm. SEM observations were made using a ThermoFisher Quattro ESEM at the Electron Microscopy Laboratory (EML), Peking University (PKU).

2.4. Statistical methods

Digital BF TEM images and high-resolution secondary electron images were used for statistical analysis of the morphologies and sizes of magnetite particles. Each particle was fitted with the minimum outer rectangle. The rectangle length and width were measured manually using ImageJ software as the particle length and width, respectively. Histograms were obtained by plotting counts of particles against particle length, and the width/length ratio. The Shapiro-Wilk test, Kolmogorov-Smirnov test, and Quantile-Quantile plots were performed to check distributions of particle sizes and their differences. Plots of particle length versus width with confidence ellipse were calculated for investigating possible crystallographic characteristics.

2.5. Micromagnetic simulations

Micromagnetic simulations were carried out using the finite-element (FE) micromagnetic modelling package MERRILL version 1.3.5 (Ó Conbhuí et al., 2018) to determine possible magnetic domain states of typical giant magnetite crystals. The modelled crystal geometries for individual particles were created based on observed morphologies and dimensions in this study. The FE software Trelis (Trelis, 2021) was used to mesh micromagnetic models with a mesh size of 9 nm, and the ParaView (Ahrens et al., 2005) was used to visualize simulation results. The [110] crystallographic direction for the spearhead model and [111] crystallographic direction for other crystal models were set to be parallel to the elongation direction, consistent with observations in this study and previous reports (Schumann et al., 2008; Chang et al., 2012). Here, a saturation field of 1 T was applied to modelled crystal along the axis of particle elongation, and then the magnetic domain state of saturation isothermal remanent magnetization (SIRM) was calculated at zero field.

3. Results

3.1. Magnetic properties of bulk sediments

Magnetic analyses for typical samples indicate that bulk sediments have similar magnetic properties at Sites U1409 and U1403 during different PETM time intervals (Fig. 3). Three main magnetic components are isolated from the IRM acquisition curves (Fig. 3a, b). The lowest coercivity component (blue) with a broad distribution represents detrital magnetite (Egli, 2004). The other two distinct IRM components with narrow coercivity distributions correspond to the biogenic soft (purple) and biogenic hard (green) (Egli, 2004). The presence of magnetofossils is confirmed by the dominant non-interacting domain state (SD) central ridge component along the H_c axis of the FORC diagrams (Fig. 3c, d) (Egli, 2010).

3.2. Morphological features of giant magnetofossils

SEM and TEM observations for typical samples from Sites U1409 and U1403 reveal the abundant occurrence of variable types of magnetofossils before, during, and after the PETM at two distinct palaeodepths in the North Atlantic (Figs. 4, 5 and Figs. S1-S5). We imaged, counted, and analyzed more than 9000 magnetofossil crystals and divided them into seven groups (Fig. 6) according to their grain sizes and morphologies, including four types of giant magnetofossils (spearhead, spindle, needle, and giant bullet) (Table S1) and three types of other magnetofossils (small needle, bullet, and other conventional magnetofossils) (Table S2).

The length distribution histograms for all needle-shaped (Fig. 6c) and bullet-shaped particles (Fig. 6d) both are typically bimodal with boundaries at particle length of ~400 nm. Therefore, the length boundaries of the needle and small needle, giant bullet and bullet are set to 400 nm. The category for other conventional magnetofossils is defined as a combination of cuboctahedral and elongated-prismatic magnetite crystals. The width/length ratio distribution histogram for all needle-shaped and other conventional magnetofossils (Fig. 6j) shows a bimodal distribution with a boundary at width/length ratio of ~0.3. The category for the small needle in this study is characterized by a much smaller width/length ratio (<0.3) compared with conventional elongated prisms (width/length ratio of

~0.8) (Wagner et al., 2021a, b). Length distribution histograms (Fig. 6a-e) and statistical analyses (Fig. S6 and Tables S1, S2) for the defined seven groups indicate that the crystal length of spearhead, spindle, and small needle has a normal distribution. Grain sizes for the needle and giant bullet show approximately normal distributions, while bullet and other conventional magnetofossils are non-normal distributions.

All reported four types of giant magnetofossils have been identified in our samples. The spearhead-like crystals have variable sizes of stalks and tails (Fig. 4a-c). Some spearheads do not have tails (Fig. 4d, j and Fig. S5). Spearhead particles have a pyramid-like structure at the tip, while the cross-section for crystals without tails is elliptical at the end of the particle opposite to the tip (Fig. 4d, j and Fig. S5). Some spearheads are characterized by circumferential features and broken parts on their stalks (Fig. 4d and Fig. S3f, i). TEM observations also show two types of spearheads: one with tails and one without tails (Fig. 5a). The length of spearheads ranges from ~0.6 to 3.5 μm, while their width ranges from ~0.25 to 1.9 μm (Table S1). Spindles have a length of ~0.65–2.8 μm and a width of ~0.16–0.7 μm with tapers at both ends (Fig. 4d, e, j). Needles have a length of 0.4–2 μm and a narrow width of ~0.07–0.18 μm (Figs. 4f, g and 5b). Some giant bullet-shaped crystals have a flat cross-section at the tail section and a dome at the tip (Figs. 4h, i and 5c), similar to some conventional bullet-shaped magnetofossils. The observed giant bullet-shaped particle size has a length of 0.4–2.6 μm and a width of ~0.1–0.94 μm. We also observe that giant bullets and needles commonly have a bilateral cross-section in the 2 dimensions or a conical shape in the 3 dimensions at their tail section (Fig. 5b, c), consistent with previous observations (Schumann et al., 2008; Chang et al., 2012). Giant magnetofossils were observed as isolated particles or aggregates without any clear in-situ structures in the studied magnetic extracts (Figs. 4 and 5).

3.3. Crystallographic characteristics of giant magnetofossils

SAED, HRTEM, and EDS analyses for all types of giant and conventional magnetofossil crystals

indicate a crystal structure and chemical composition consistent with magnetite (Fig. 5 and Fig. S7). A primitive cubic superlattice was identified in the SAED pattern of one spearhead-shaped crystal (Fig. 5a), suggesting that this magnetite particle is partially oxidized to maghemite with ordered superstructure reflections due to vacancy ordering (Zhou et al., 1999). An HRTEM image of the tip of a single spearhead shows two sets of orthogonal lattice fringes with a *d*-spacing of ~0.29 nm that corresponds to the {220} planes of magnetite (Fig. 5a). One spearhead without tail elongates along the [311] crystal direction of magnetite. A needle particle shows a *d*-spacing of 0.484 nm, corresponding to a {111} plane that is nearly perpendicular to the elongation direction (Fig. 5b). Analysis of lattice fringes for 8 needles suggests that the prominent elongation direction in giant needles is parallel to the [111] crystallographic direction of magnetite. The {111} plane with 0.484 nm *d*-spacing for a giant bullet crystal (Fig. 5c) is nearly perpendicular to the crystal elongation direction, similar to those for needles.

3.4. Micromagnetic simulations of giant magnetofossil crystals

The size and morphology of giant magnetofossils indicate that spearheads lie within the multidomain (MD) region, needles in the SD region, spindles and giant bullets mostly in the vortex state zone, respectively (Muxworthy and Williams, 2009) (Fig. 7). Twenty-five individual particles of different grain sizes were selected for micromagnetic simulations to better characterise domain structures of giant magnetite crystals (Fig. 8, Fig. S8 and Table S3). Simulations of giant magnetite crystals indicate that all spearheads have MD structures (Fig. 8a-e). Spindles (Fig. 8f-j) and needles (Fig. 8k-o) have SD structures and a single needle crystal with a length of 1.19 μm (Fig. 8l) has the vortex state at both ends of the particle. Giant bullets for all modelled grain sizes have single vortex structures in the center (Fig. 8p-t). All small needles have SD structures (Fig. S8).

4. Discussions

241 *4.1. Magnetic domain state of giant magnetite particles*

242 Magnetic domain states of the four types of isolated giant magnetite particles in the magnetic
243 domain state phase diagram (Fig. 7) (Muxworthy and Williams, 2009) are consistent with
244 micromagnetic modelling results (Fig. 8) (Chang et al., 2012; Wagner et al., 2021a), while some giant
245 magnetite crystals show different domain structures depending on their variations in grain size. In
246 general, spearheads have MD structures (Figs. 7 and 8a-e) because of their large mean grain size (~1.8
247 μm) and width/length ratio (~0.49). Spindles lie in the vortex state in the domain state phase diagram
248 (Fig. 7) but show SD structures from micromagnetic simulations (Fig. 8f-j), which are attributed to
249 their typical tapers at both ends. Small needles and needles both have strongly SD behaviour (Figs. 7,
250 8k-o and Fig. S8) because of their ultra-low width/length ratio of <0.3 (Fig. 6h). All spindles and
251 needles have the flower remanent magnetization state at both ends (Fig. 8f-o and Fig. S8), similar to
252 uniaxial particles in the size of 70–80 nm (Tauxe et al., 2002). Giant bullets are vortex states (Figs. 7
253 and 8p-t) as individual crystals but may adopt stable SD properties when arranged into a chain
254 configuration (Chang et al., 2012). It should be noted that the domain states of magnetic mineral grains
255 depend on the magnitude and direction of the external magnetic field, as well as the starting domain
256 configurations. In this study, our micromagnetic models simulated magnetic domain states of SIRM
257 along the axis of particle elongation, and there are other possible domain states if the applied external
258 magnetic field is changed.

259 Wagner et al. (2021a) suggested that high-resolution FORC measurements can provide a
260 prominent central ridge offset between 120 and 210 mT to detect in-situ needles due to their ultra-high
261 coercivity. But this method may not apply to other giant magnetite crystals in bulk sediments (Wagner
262 et al., 2021a) because the coercivity peak of MD (spearhead) and vortex (giant bullet) in FORC
263 diagrams likely occur at relatively low values (Roberts et al., 2014), overlapping with detrital and
264 conventional biogenic magnetite crystals. Although simulated results indicate all sizes of spindles are

SD-like needles (Fig. 8f-j), their coercivity distributions in FORC diagrams are still unknown. In this study, biogenic soft and hard components contribute to the FORC central ridge along the H_c axis ranging from 0 to 80 mT (Fig. 3c, d). We failed to distinguish the high-coercivity contribution of needles (>120 mT) from the FORC central ridge following Wagner et al. (2021a), probably because the resolution of the FORC measurements in our measurements was not high enough or the concentration of needles in our studied sediment samples is relatively low.

4.2. Further evidence for a biogenic origin of giant magnetite particles

Because no modern organisms have been found to biomineralize giant magnetite particles or analogs, much effort has been put into investigating the origin of these unusual crystals. Schumann et al. (2008) suggested that giant magnetite particles exhibit chemical composition, lattice perfection, and oxygen isotopes consistent with an aquatic origin, similar to magnetosome crystals produced by magnetotactic bacteria (MTB). Spearhead-like particles feature a complex and anisotropic morphology with low-temperature isotopic composition (Schumann et al., 2008). Variation of the stalk and spearhead sizes of spearhead-like crystals indicated an asymmetric size variance and allometric growth (Schumann et al., 2008). Chang et al. (2012) suggested that giant bullet- and needle-like crystals may be counterparts to conventional biogenic magnetite because of their high similarity in morphologies. Nevertheless, the origin of giant magnetite crystals is still poorly understood since their discovery.

Grain size and morphological analysis of all types of giant magnetite particles are made to investigate possible phases of crystal growth and their origin (Fig. 9). Each type of giant magnetite particle lies in a characteristic region of the domain-state phase diagram (Fig. 9a). All spearheads have a pyramid-like structure, and some have different sizes of stalks without tails (Fig. 4d, j and S5), possibly associated with different crystal growth stages. Circumferential features and broken parts on spearhead stalks (Fig. 4d and Fig. S3f, i) are perpendicular to the crystal elongation direction, supporting previous observations that spearhead fragments parted along the {220} plane (Schumann

et al., 2008). These results likely indicate that the direction of crystal growth for spearheads is their elongated direction. We speculate that the pyramid-like structure of spearheads forms first, followed by a continuous growth lengthwise to form the stalk and tail (Fig. S9a-c). The shape of the confidence ellipse for spindles is flat, with its elongation nearly parallel to the crystal length direction (Fig. 9a). Spindles have a relatively narrow width dispersion compared with their length. Our observations reveal that morphologies for spindles maintain consistency during crystal growth, in contrast to spearhead-shaped particles. Spindles tend to grow along the crystal elongation direction within a relatively small width range (Fig. S9d-f).

The orientation of the confidence ellipse for small needles and needles is quite different (Fig. 9b), indicating that these two types of magnetite particles likely have different patterns of crystal growth. Small needles grow in an isotropic form with a width/length ratio close to 0.26 up to a median length of ~220 nm (Fig. S10a, b). Needles maintain a restricted width of ~100 nm and mainly grow in length (i.e., mostly along the [111] direction) to a median length of ~830 nm, with some particles growing to ~1.5–2 μm long (Fig. S10c, d). The fitted sigmoid function (Fig. 9b, $R^2 = 0.78$) for all needle-shaped crystals seems to indicate a potential linkage between small needles and needles (Fig. S10). Vali and Kirschvink (1991) described the bacterial magnetosome crystals of ~300 nm in length and ~30 nm in width from the bacterium with a length of 4 μm, almost the same as partial small needles in our observations (Fig. S1c, d). However, the origin of these small needles and needles remains unknown due to limited reports.

The bullets and giant bullets have a similar shape of confidence ellipse, indicating a similar length-width relationship (Fig. 9b). The median length of bullets and giant bullets is ~100 nm and ~880 nm, respectively, with corresponding median widths of ~37 nm and ~310 nm. Our results indicate that all bullet-shaped magnetite particles may grow isotropically in similar length and width growth rates, with a width/length ratio of ~0.25–0.5 (Fig. S10e-h). Although we define bullets as the bullet-shaped

magnetite with a crystal length of less than 400 nm (Fig. 6d), several types of bullet-shaped magnetofossils with different grain sizes and morphologies are observed in our samples. The bullets with crystal length of <~200 nm (Figs. S1a and S10e) and crystal length ranging from 200 nm to 400 nm (Figs. S1b and S10f) might be produced by magnetotactic bacteria and eukaryotes, respectively, consistent with some reports of bullet-shaped magnetite within living magnetotactic organisms (Amor et al., 2020; Li et al., 2010, 2019, 2020; Leão et al., 2020).

Compared to conventional magnetofossils (Amor et al., 2020; Arató et al., 2005; Devouard et al., 1998), the grain size and width/length ratio distributions of giant magnetite crystals (Fig. 6) are insufficient to confirm their origin. However, it is unlikely that these large magnetite microparticles with typical morphology and directional growth formed through any inorganic process, but rather are biologically controlled. Unlike spearheads and spindles with no analogues, needles and giant bullets appear to have a potential linkage with some known magnetite crystals produced by living magnetotactic bacteria or eukaryotes. Our data seem to provide additional clues for a biogenic origin of giant magnetite crystals, supporting previous results based on oxygen isotope measurements of a spearhead-like particle (Schumann et al., 2008).

4.3. Hyperthermal conditions do not drive formation of giant magnetite crystals

Previous studies indicate that giant magnetofossils were exclusively associated with past global warming periods (e.g., during the PETM and the MECO) (Schumann et al., 2008; Kopp et al., 2009; Chang et al., 2012, 2018; Wang et al., 2015; Wagner et al., 2021a, b), suggesting that extreme hyperthermal conditions, e.g. high iron bioavailability combined with an expanded suboxic zone may drive biomineralization of giant magnetite in eukaryotes. A sharp lithological change often occurred at the base of PETM, such as in pelagic cores on the Walvis Ridge (Zachos et al., 2005) and in neritic sections on the North Atlantic continental shelf (e.g., Kopp et al., 2007, 2009; Lippert and Zachos, 2007), where carbonate-rich sediments transit to clay intervals with a sharp increase in iron

concentration. It was reported that oceanic deoxygenation (Chang et al., 2018) and increase in iron concentration (Zachos et al., 2005) occurred from the onset to the CIE peak in the South Atlantic.

We observe the presence of giant magnetofossils at both sites very early before (>700 ky earlier than the PEB, Palaeocene-Eocene boundary), during, and very late after (>300 ky later than the PEB) the PETM (Fig. 2 and Table 1), indicating that giant magnetofossils were not uniquely associated with hyperthermal events. SEM observations for a sample with an approximate age of 70 Ma at Site U1403 (Table 1) undoubtedly demonstrate the common presence of giant magnetofossils outside the hyperthermal periods. All observations for typical giant magnetofossil morphologies are nearly identical to those reported previously (Schumann et al., 2008; Kopp et al., 2009; Chang et al., 2012; Wang et al., 2015; Wagner et al., 2021a, b). Combined with previous observations on samples within the CIE body on the New Jersey continental shelf (Schumann et al., 2008; Kopp et al., 2009; Wang et al., 2015; Wagner et al., 2021a, b), our results indicate that giant magnetofossils were likely very common in shallow and deep marine environments in the North Atlantic, together with the presence of bullets, small needles, and other conventional biogenic magnetite.

Our statistical results suggest that the grain sizes of spearheads in New Jersey appear to be larger than that at Sites U1409 and U1403 (Fig. 7 and Fig. S11a), while the other three types of giant magnetite crystals are not statistically significant in terms of crystal dimensions due to the small number of counted particles (Fig. 7 and Fig S11b-d). Statistical results (Figs. S11, S12 and Tables S4, S5) reveal that spearheads at Site U1409 have a similar particle length to that at Site U1403, whereas the particle length of needles and giant bullets at Site U1409 appears to be slightly larger than that at Site U1403. Given there is no solid evidence for a biogenic origin of giant magnetite crystals up to this day, potential environmental effects on the variation of the grain sizes are unknown. Further investigations are highly needed to unravel key environmental controls of these mysterious giant magnetite crystals.

5. Conclusions and outlook

We have identified abundant occurrence of four types of giant magnetite crystals before, during, and after the PETM in the North Atlantic using high-resolution TEM and SEM observations. Dimensional data and micromagnetic simulations reveal the magnetic domain states of these giant magnetite crystals with different grain sizes. The directional growth of giant bullets and needles, crystallography, and size distributions may provide additional evidence for a biogenic origin of giant magnetite grains, supporting earlier results and speculation (Schumann et al., 2008; Chang et al., 2012). The occurrence of giant magnetofossils within both PETM and non PETM intervals indicates that these mysterious magnetite crystals are not uniquely associated with past global warming periods.

These new observations advance our understanding of biotic response under major climate perturbation during ancient hyperthermal events, such as the PETM. We suspect that giant magnetite crystals may be much more common in the geological record than previously thought. Changes in the size of giant magnetite crystals may contribute to forecasting the impacts of climate perturbation on marine ecosystems in the current-future global warming.

Acknowledgements

Samples were provided by the International Ocean Discovery Program (IODP), which is sponsored by the US National Science Foundation and participating countries under management of Joint Oceanographic Institutions, Inc. We thank Shishun Wang for assistant in sampling; Xu Tang for assistance in high-resolution TEM analyses; Xiaofan Cao for suggestions in SEM sample preparations; and Li Chen for assists in high-resolution SEM analyses. This study was supported by the National Natural Science Foundation of China (NSFC grants 41974074, 42061130214, 41574060). L.C. and

R.J.H. acknowledge supports from a Royal Society-Newton Advanced Fellowship (grant NAF\R1\201096).

Data Availability Statement

All data in this study are available in the supplementary materials and at the Peking University Open Research Data Repository (https://doi.org/10.18170/DVN/OJR591).

References

Alegret, L., Arreguín-Rodríguez, G.J., Trasviña-Moreno, C.A., Thomas, E., 2021. Turnover and stability in the deep sea: Benthic foraminifera as tracers of Paleogene global change. Glob. Planet. Change 196, 103372.

Ahrens, J., Geveci, B., Law, C., 2005. ParaView: An end-user tool for large-data visualization, in: Hansen, C.D., Johnson, C.R. (Eds), The visualization handbook. Elsevier, pp. 717–731.

Amor, M., Mathon, F.P., Monteil, C.L., Busigny, V., Lefevre, C.T., 2020. Iron-biomineralization organelle in magnetotactic bacteria: function, synthesis and preservation in ancient rock samples. Environ. Microbiol. 22(9), 3611–3632.

Arató, B., Szányi, Z., Flies, C., Schüler, D., Frankel, R.B., Buseck, P.R., Pósfai, M., 2005. Crystal-size and shape distributions of magnetite from uncultured magnetotactic bacteria as a potential biomarker. Am. Miner. 90, 1233–1241.

Chang, L., Roberts, A.P., Williams, W., Fitz Gerald, J.D., Larrasoaña, J.C., Jovane, L., Muxworthy, A.R., 2012. Giant magnetofossils and hyperthermal events. Earth Planet. Sci. Lett. 351–352, 258–269.

Chang, L., Harrison, R.J., Zeng, F., Berndt, T.A., Roberts, A.P., Heslop, D., Zhao, X., 2018. Coupled microbial bloom and oxygenation decline recorded by magnetofossils during the Palaeocene-

Eocene Thermal Maximum. Nat. Commun. 9, 4007.

Devouard, B., Pósfai, M., Hua, X., Bazylinski, D.A., Frankel., R.B., Buseck, P.R., 1998. Magnetite from magnetotactic bacteria: Size distributions and twinning. Am. Miner. 83, 1387–1398.

Egli, R., 2004. Characterization of individual rock magnetic components by analysis of remanence curves, 1. Unmixing natural sediments. Stud. Geophys. Geod. 48, 391–446.

Egli, R., Chen, A.P., Winklhofer, M., Kodama, K.P., Horng, C.S., 2010. Detection of noninteracting single domain particles using first-order reversal curve diagrams. Geochem. Geophys. Geosyst. 11, Q01Z11.

Egli, R., 2013. VARIFORC: An optimized protocol for calculating non-regular first-order reversal curve (FORC) diagrams. Glob. Planet. Change 110, 302–320.

Harrison, R.J., Feinberg, J.M., 2008. FORCinel: An improved algorithm for calculating first-order reversal curve distributions using locally weighted regression smoothing. Geochem. Geophys. Geosyst. 9(5).

Kopp, R.E., Raub, T.D., Schumann, D., Vali, H., Smirnov, A.V., Kirschvink, J.L., 2007. Magnetofossil spike during the Paleocene-Eocene thermal maximum: Ferromagnetic resonance, rock magnetic, and electron microscopy evidence from Ancora, New Jersey, United States. Paleoceanography 22, PA4103.

Kopp, R.E., Schumann, D., Raub, T.D., Powars, D.S., Godfrey, L.V., Swanson-Hysell, N.L., Maloof, A.C., Vali, H., 2009. An Appalachian Amazon? Magnetofossil evidence for the development of a tropical river-like system in the mid-Atlantic United States during the Paleocene-Eocene thermal maximum. Paleoceanography 24, PA4211.

Leão, P., Le Nagard, L., Yuan, H., Cypriano, J., Da Silva-Neto, I., Bazylinski, D.A., Acosta-Avalos, D., de Barros, H.L., Hitchcock, A.P., Lins, U., Abreu, F., 2020. Magnetosome magnetite biomineralization in a flagellated protist: evidence for an early evolutionary origin for

magnetoreception in eukaryotes. Environ. Microbiol. 22(4), 1495–1506.

Li, J., Pan, Y., Liu, Q., Yu-Zhang, K., Menguy, N., Che, R., Qin, H., Lin, W., Wu, W., Petersen, N., Yang, X., 2010. Biomineralization, crystallography and magnetic properties of bullet-shaped magnetite magnetosomes in giant rod magnetotactic bacteria. Earth Planet. Sci. Lett. 293, 368–376.

Li, J., Zhang, H., Liu., P., Menguy, N., Roberts, A.P., 2019. Phylogenetic and structural identification of a novel magnetotactic Deltaproteobacterium strain WYHR-1 from a freshwater lake. Appl. Environ. Microbiol. 85, e00731.

Li, J., Menguy, N., Roberts, A.P., Gu, L., Leroy, E., Bourgon, J., Yang, X., Zhao, X., Liu, P., Changela, H.G., Pan, Y., 2020. Bullet-Shaped Magnetite Biomineralization Within a Magnetotactic Deltaproteobacterium: Implications for Magnetofossil Identification. J. Geophys. Res. Biogeosci. 125.

Lippert, P.C., Zachos, J.C., 2007. A biogenic origin for anomalous fine-grained magnetic material at the Paleocene-Eocene boundary at Wilson Lake, New Jersey. Paleoceanography 22, PA4104.

Maxbauer, D.P., Feinberg, J.M., Fox, D.L., 2016. MAX UnMix: A web application for unmixing magnetic coercivity distributions. Comput. Geosci. 95, 140–145.

McInerney, F.A., Wing, S.L., 2011. The Paleocene-Eocene Thermal Maximum: A Perturbation of Carbon Cycle, Climate, and Biosphere with Implications for the Future. Annu. Rev. Earth Planet Sci. 39, 489–516.

Muxworthy, A.R., Williams, W., 2009. Critical superparamagnetic/single-domain grain sizes in interacting magnetite particles: implications for magnetosome crystals. J. R. Soc. Interface 6, 1207–1212.

Norris, R.D., Wilson, P.A., Blum, P., the Expedition 342 Scientists, 2012. Proc. IODP Vol. 342.

Ó Conbhuí, P., Williams, W., Fabian,K., Ridley, P., Nagy, L., Muxworthy, A.R., 2018. MERRILL:

Micromagnetic earth related robust interpreted language laboratory. Geochem. Geophys. Geosyst. 19, 1080–1106.

Penman, D.E., Turner, S.K., Sexton, P.F., Norris, R.D., Dickson, A.J., Boulila, S., Ridgwell, A., Zeebe, R.E., Zachos, J.C., Cameron, A., Westerhold, T., Röhl, U., 2016. An abyssal carbonate compensation depth overshoot in the aftermath of the Palaeocene–Eocene Thermal Maximum. Nat. Geosci. 9, 575–580.

Petrizzo, M.R., 2007. The onset of the Paleocene–Eocene Thermal Maximum (PETM) at Sites 1209 and 1210 (Shatsky Rise, Pacific Ocean) as recorded by planktonic foraminifera. Mar. Micropaleontol. 63, 187–200.

Roberts, A.P., Pike, C.R., Verosub, K.L., 2000. First order reversal curve diagrams: a new tool for characterizing the magnetic properties of natural samples. J. Geophys. Res. 115(B12), 28461–28475.

Roberts, A.P., Heslop, D., Zhao, X., Pike, C.R., 2014. Understanding fine magnetic particle systems through use of first-order reversal curve diagrams. Rev. Geophys. 52, 557–602.

Schumann, D., Raub, T.D., Kopp, R.E., Guerquin-Kern, J., Wu, T., Rouiller, I., Smirnov, A.V., Sears, S.K., Lucken, U., Tikoo, S.M., Hesse, R., Kirschvink, J.L., Vali, H., 2008. Gigantism in unique biogenic magnetite at the Paleocene-Eocene Thermal Maximum. Proc. Natl. Acad. Sci. USA 105, 17648–17653.

Sluijs, A., Bowen, G.J., Brinkhuis, H., Lourens, I.J., Thomas, E., 2007. The Palaeocene–Eocene thermal maximum super greenhouse: Biotic and geochemical signatures, age models and mechanisms of global change. In: Williams, M., Haywood, A.M., Gregory, F.J. and Schmidt, D.N. (eds) Deep- Time Perspectives on Climate Change: Marrying the Signal from Computer Models and Biological Proxies. Micropalaeontological Society, Special Publications. Geological Society, London, 323–349.

480 Tauxe, L., Bertram, H.N., Seberino, C., 2002. Physical interpretation of hysteresis loops:
481 Micromagnetic modeling of fine particle magnetite. Geochem. Geophys. Geosysr. 3(10), 1055.
482 Thomas, E., Shackleton, N.J., 1996. The Paleocene-Eocene benthic foraminiferal extinction and stable
483 isotope anomalies. Geological Society, London, Special Publications 101, 401–441.
484 Thomas, E., 2003. Extinction and food at the sea floor: A high-resolution benthic foraminiferal record
485 across the Initial Eocene Thermal Maximum, Southern Ocean Site 690. Causes and consequences
486 of globally warm climates of the Paleogene: Geological Society of America Special Paper 369,
487 319–332.
488 Thomas, E., 2007. Cenozoic mass extinctions in the deep sea: What perturbs the largest habitat on
489 Earth? Causes and Consequences: Geological Society of America Special Paper 424, 1–23.
490 Tiernery, J.E., Poulsen, C.J., Montañez, I.P., Bhattacharya, T., Feng, R., Ford, H.L., Hönisch, B., Inglis,
491 G.N., Petersen, S.V., Sagoo, N., Tabor, C.R., Thirumalai, K., Zhu, J., Burls, N.J., Foster, G.L.,
492 Goddéris, Y., Huber, B.T., Ivany, L.C., Turner, S.K., Lunt, D.J., McElwain, J.C., Mills, B.J.W.,
493 Otto-Bliesner, B.L., Ridgwell, A., Zhang, Y., 2020. Past climates inform our future. Science 370
494 (6517).
495 Trelis, 2021. (Version 2021.3) [computer software] Coreform LLC. Retrieved from
496 http://coreform.com
497 Vali, H., Kirschvink, J.L., 1991. Observations of magnetosome organization, surface structure, and
498 iron biomineralization of undescribed magnetic bacteria: environmental speculations, in: Frankel,
499 R.B., Blakemore, R.P. (Eds.), Iron Biominerals. Springer US, pp. 97–115.
500 Wagner, C.L., Egli, R., Lascu, I., Lippert, P.C., Livi, K.J.T., Sears, H.B., 2021a. In situ magnetic
501 identification of giant, needle-shaped magnetofossils in Paleocene-Eocene Thermal Maximum
502 sediments. Proc. Natl. Acad. Sci. USA 118.
503 Wagner, C.L., Lascu, I., Lippert, P.C., Egli, R., Livi, K.J.T., Sears, H.B., 2021b. Diversification of iron-

biomineralizing organisms during the Paleocene-Eocene Thermal Maximum: evidence from quantitative unmixing of magnetic signatures of conventional and giant magnetofossils. Paleoceanography and Paleoclimatology 36.

Wang, H., Wang, J., Chen-Wiegart, Y.C., Kent, D.V., 2015. Quantified abundance of magnetofossils at the Paleocene-Eocene boundary from synchrotron-based transmission X-ray microscopy. Proc. Natl. Acad. Sci. USA 112, 12598–12603.

Zachos, J.C., Röhl, U., Schellenberg, S.A., Sluijs, A., Hodell, D.A., Kelly, D.C., Thomas, E., Nicolo, M., Raffi, I., Lourens, L.J., McCarren, H., Kroon, D., 2005. Rapid acidification of the ocean during the Paleocene-Eocene thermal maximum. Science 308, 1611–1615.

Zachos, J.C., Dickens, G.R., Zeebe, R.E., 2008. An early Cenozoic perspective on greenhouse warming and carbon-cycle dynamics. Nature 451, 279–283.

Zhou, W., Peacor, D.R., Van der Voo, R., Mansfield, J.F., 1999. Determination of lattice parameter, oxidation state, and composition of individual titanomagnetite/titanomaghemite grains by transmission electron microscopy. J. Geophys. Res. 104, 17689–17702.

Figures

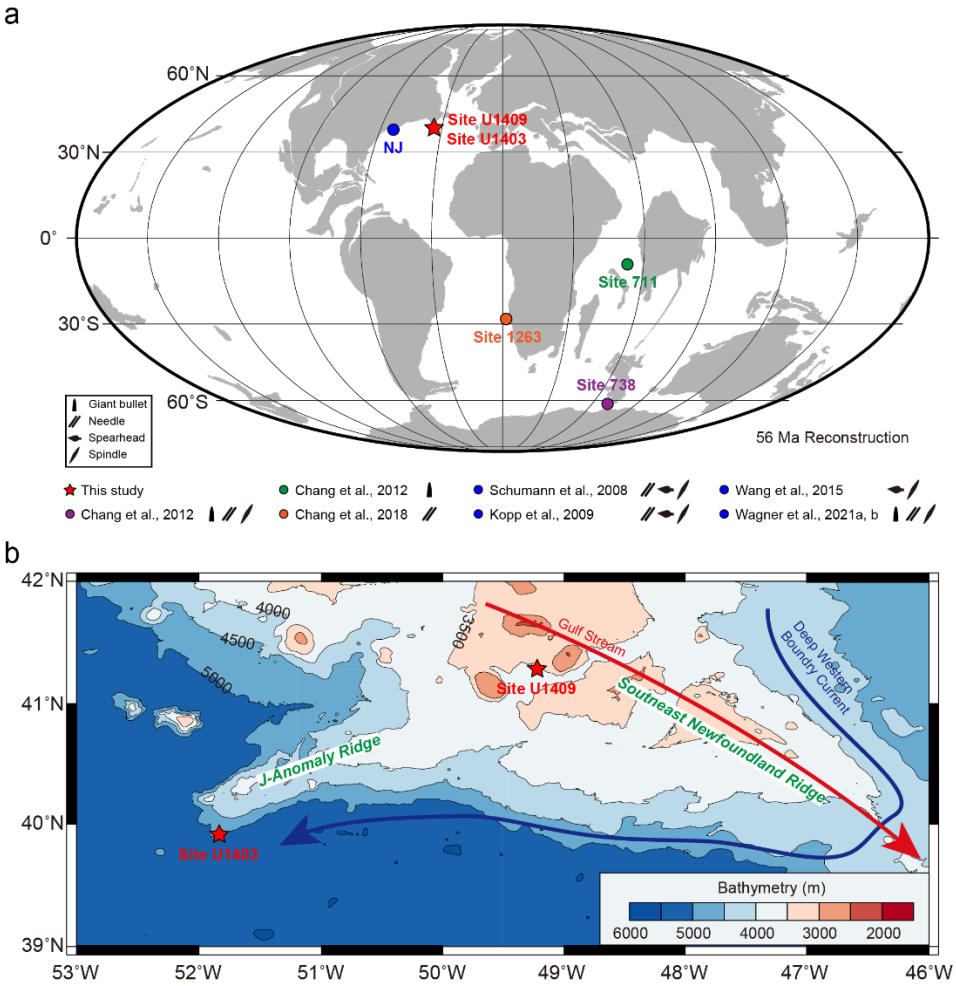

Fig. 1. Location of the studied IODP sites (U1403 and U1409) from the North Atlantic. (a) A map of plate tectonic reconstruction at 56 Ma obtained from the Ocean Drilling Stratigraphic Network (ODSN) database (http://www.odsn.de). Red stars represent the site location in this study. Solid circles of different colors show the site location from previous studies that identified giant magnetofossils. The small cartoon drawings of four different solid shapes represent giant bullet, needle, spearhead, and spindle, respectively. NJ, New Jersey. (b) Current bathymetric map of the studied site area. Bathymetric data are from the National Oceanic and Atmospheric Administration (NOAA). Blue and red arrows represent Deep Western Boundary Current and Gulf Stream, respectively.

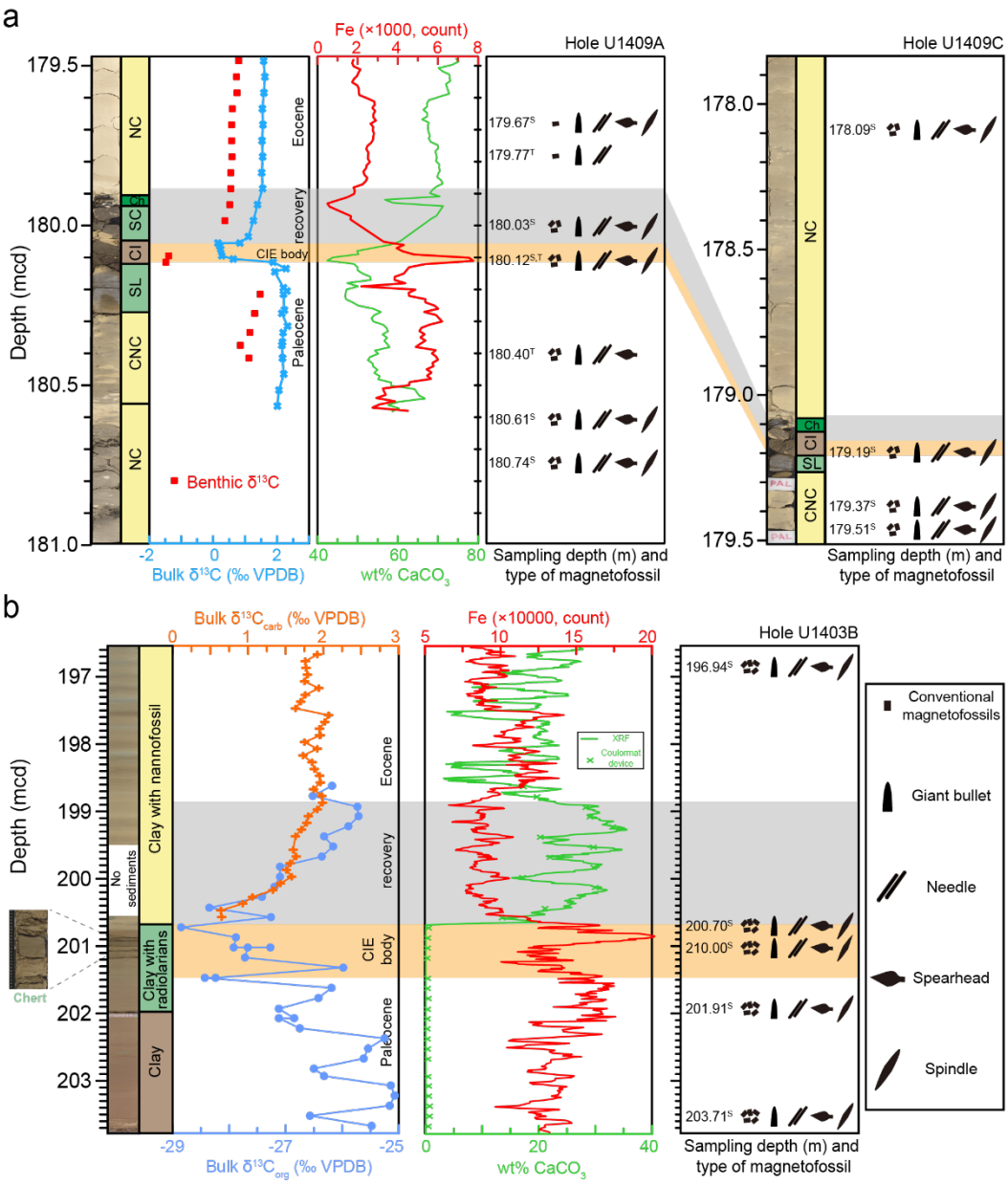

Fig. 2. Core photo, lithology, $\delta^{13}C$, wt% $CaCO_3$, Fe concentration, and the identified magnetofossils in sediments from IODP Exp. 342. (a) Site U1409 (~2913 m palaeodepth) and (b) Site U1403 (~4374 m palaeodepth). Ch, chert; Cl, claystone; CNC, clayey nannofossil chalk; NC, nannofossil chalk; SC, siliceous claystone; SL, siliceous limestone. $\delta^{13}C_{org}$: organic carbon. Core profile data are from Norris et al. (2012) and Penman et al. (2016). Yellow and grey areas represent the CIE body and recovery phases of the PETM, respectively. Different shaped cartoons represent distinct types of magnetite crystals.

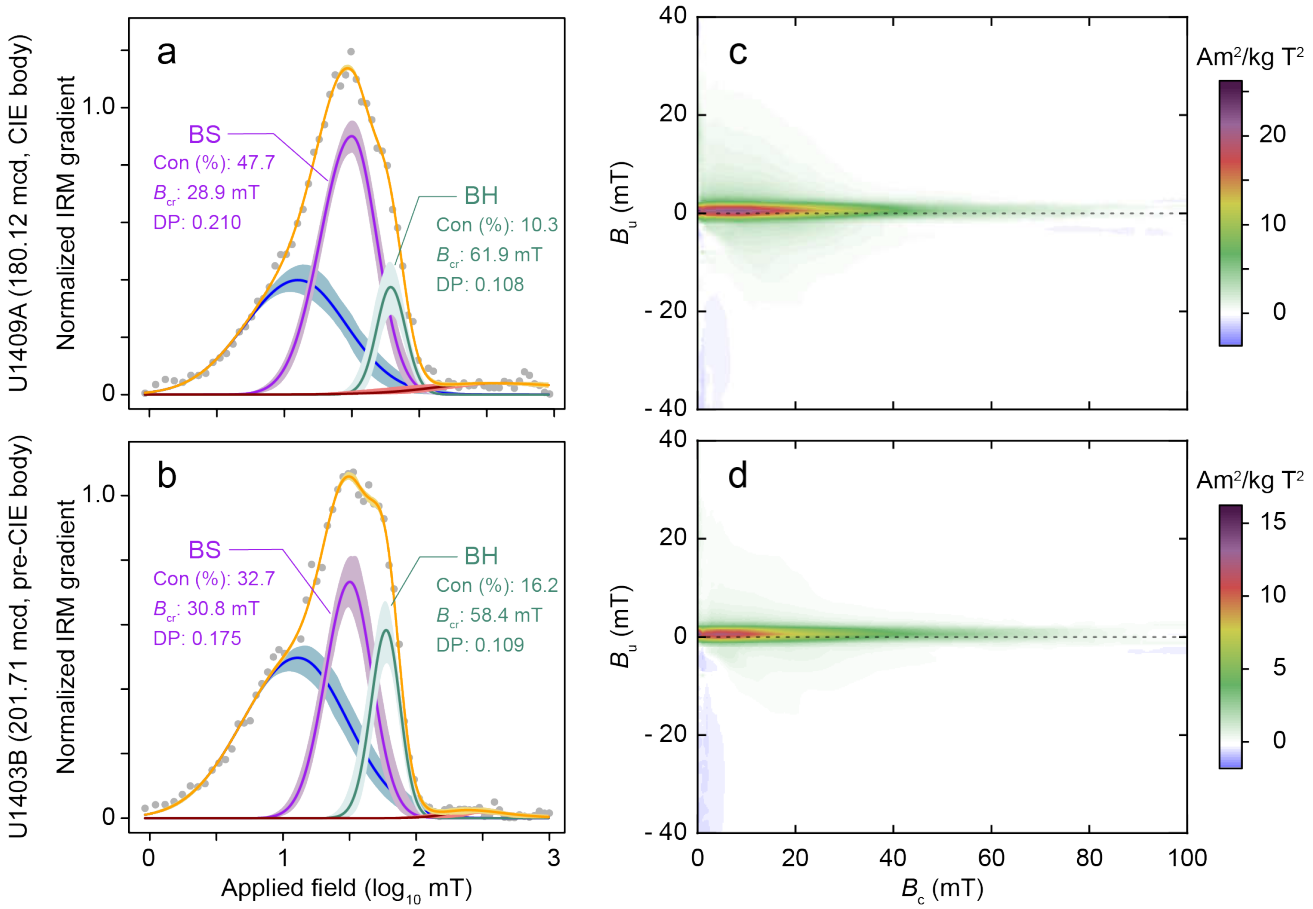

Fig. 3. Magnetic properties for typical samples from IODP Sites U1409 and U1403 across the PETM. (a) and (b), IRM coercivity decomposition analysis for samples from Holes U1409A and U1403B. The derivative of the measured data is plotted as grey solid circles and fitted with the orange line. Blue, purple, and green lines reflect three decomposed magnetic components including coarse-grained magnetite, biogenic soft (BS), and biogenic hard (BH) components, respectively. Magnetic contribution (%), the coercivity of remanence (B_{cr}), and the dispersion parameter (DP) for the BS and BH are included in (a) and (b). The shaded area reflects the 95% confidence level. (c) and (d), FORC diagrams for samples from Hole U1409A and U1403B. The VARIFORC smoothing parameters (Egli, 2013) are used: $S_{c0} = 4$, $S_{c1} = 7$, $S_{u0} = 3$, $S_{u1} = 7$, and $\lambda_c = 0.1$, $\lambda_u = 0.1$.

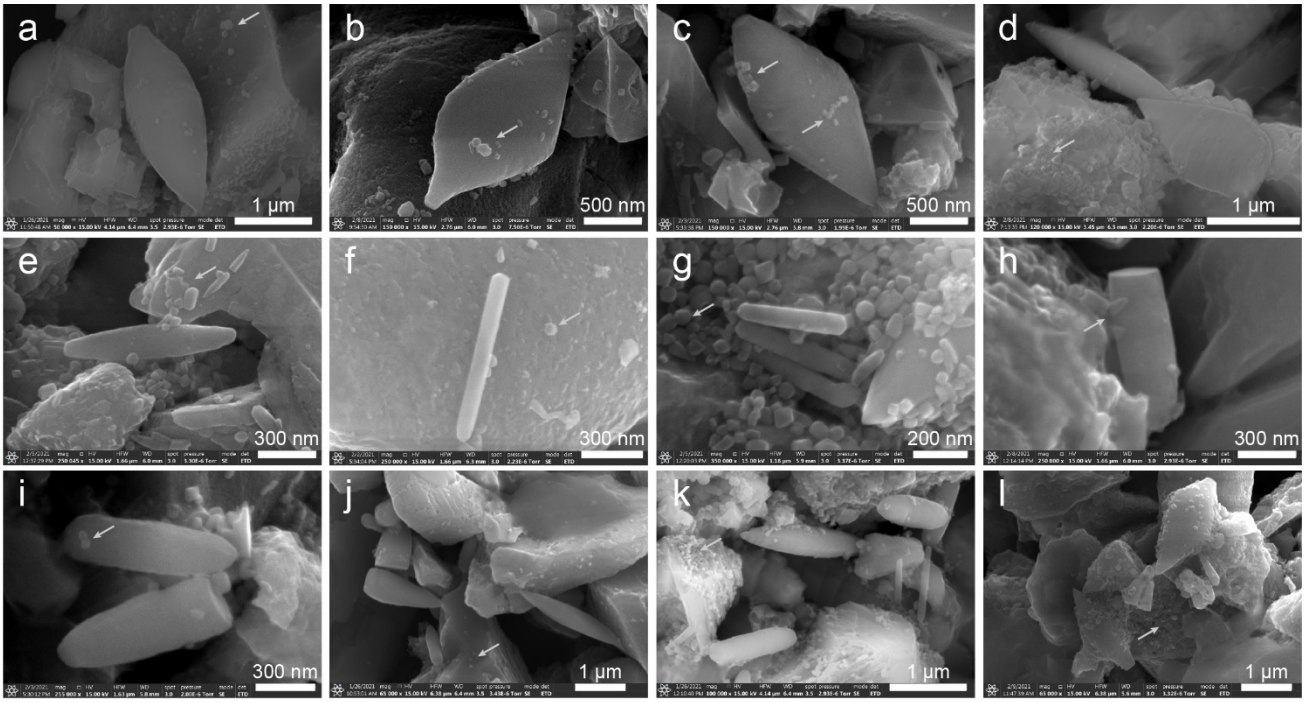

Fig. 4. SEM images of four types of giant magnetofossils. (a-d) Spearheads with different sizes of tails, and a circumferential feature in stalk sectors (d). Spindles (d and e), needles (f and g), giant bullets (h and i), and aggregates of giant magnetofossils (j-l). White arrows in each SEM image point to the other conventional magnetofossils.

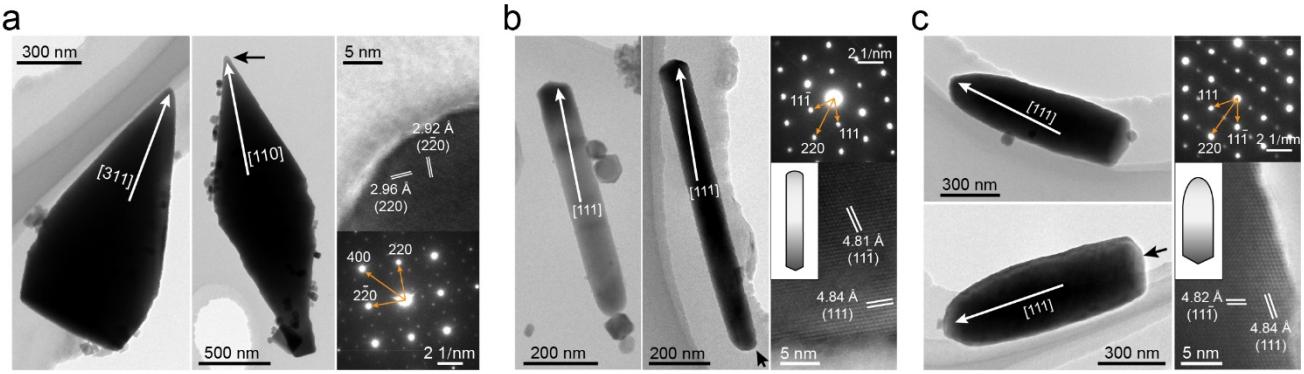

Fig. 5. TEM analysis of giant magnetofossils. Low-resolution bright-field TEM images, HRTEM images, and SAED patterns for (a) spearheads, (b) needles, and (c) giant bullets. The crystallographic lattice direction [hkl] is indicated by white arrows. Positions of HRTEM and SAED are indicated by black arrows. Insets in the HRTEM images of (b) needle and (c) giant bullet show models of crystal habits with a similar two sharp edge end. The sharp end in the schematic diagram is amplified compared to actual particles. Lattice fringe values and the corresponding Miller indices (hkl) for all particles correspond to those of magnetite. The single spearhead is partially oxidized magnetite verified by superlattice reflections in the SAED pattern (a) (Zhou et al., 1999).

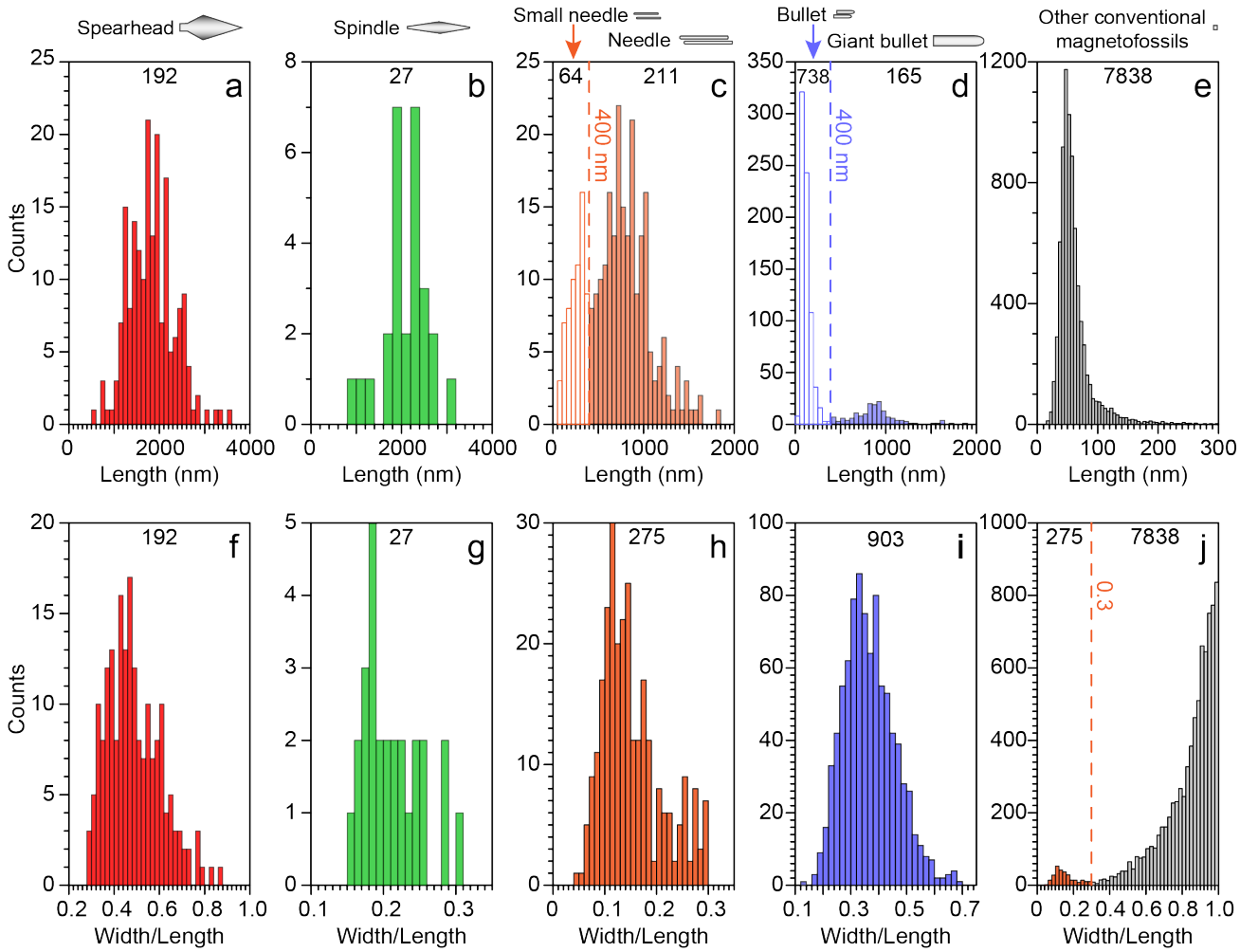

Fig. 6. Histograms for counted magnetite particles of all types and sizes. The crystal length distributions (a-e) and width/length ratio distributions (f-j) are plotted for spearheads, spindles, all needle-shaped crystals, all bullet-shaped crystals, and other conventional magnetofossils, respectively. The length distribution histograms for all needle-shaped (c) and bullet-shaped (d) crystals both are typically bimodal, which are subdivided into two humps at the length of ~400 nm. The crystal length of small needles and bullets is less than 400 nm, while that of needles and giant bullets is larger than 400 nm. The other conventional magnetofossils here include cuboctahedral and elongated-prismatic magnetite crystals. Histogram of the width/length ratio distribution for all needle-shaped particles and other conventional magnetofossils (j) indicates two distributions divided at the width/length ratio of ~0.3. The number of counted particles for each group is indicated in each plot.

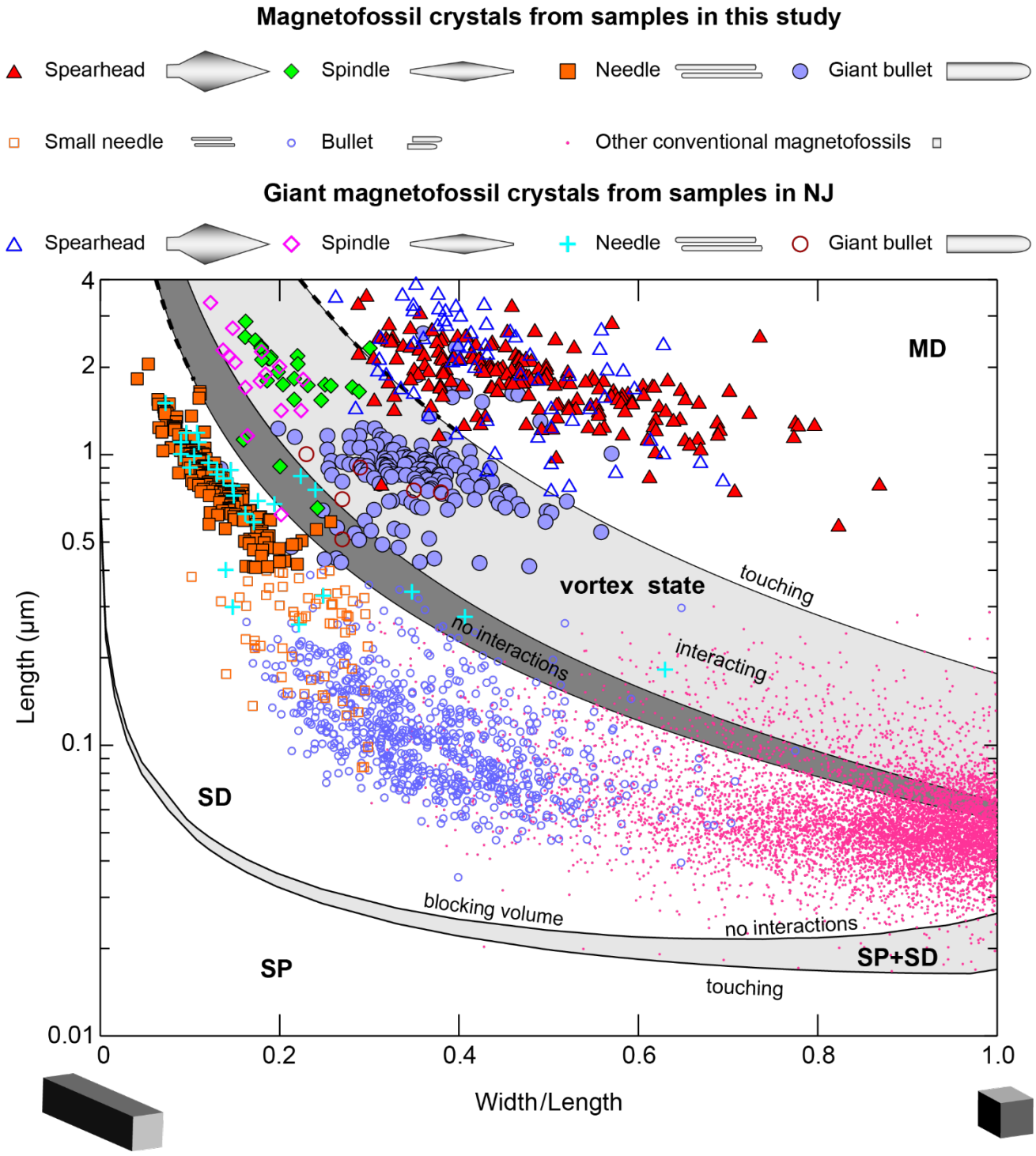

578

579 Fig. 7. Dimensional data of all types of magnetofossil crystals in samples at Sites U1409 and U1403

580 plotted in the domain state phase diagram. Dimensional data for giant magnetofossils within samples

581 in the NJ are from Schumann et al. (2008), Wang et al. (2015), and Wagner et al. (2021a). The

582 theoretical domain state diagram is from Muxworthy and Williams (2009).

583

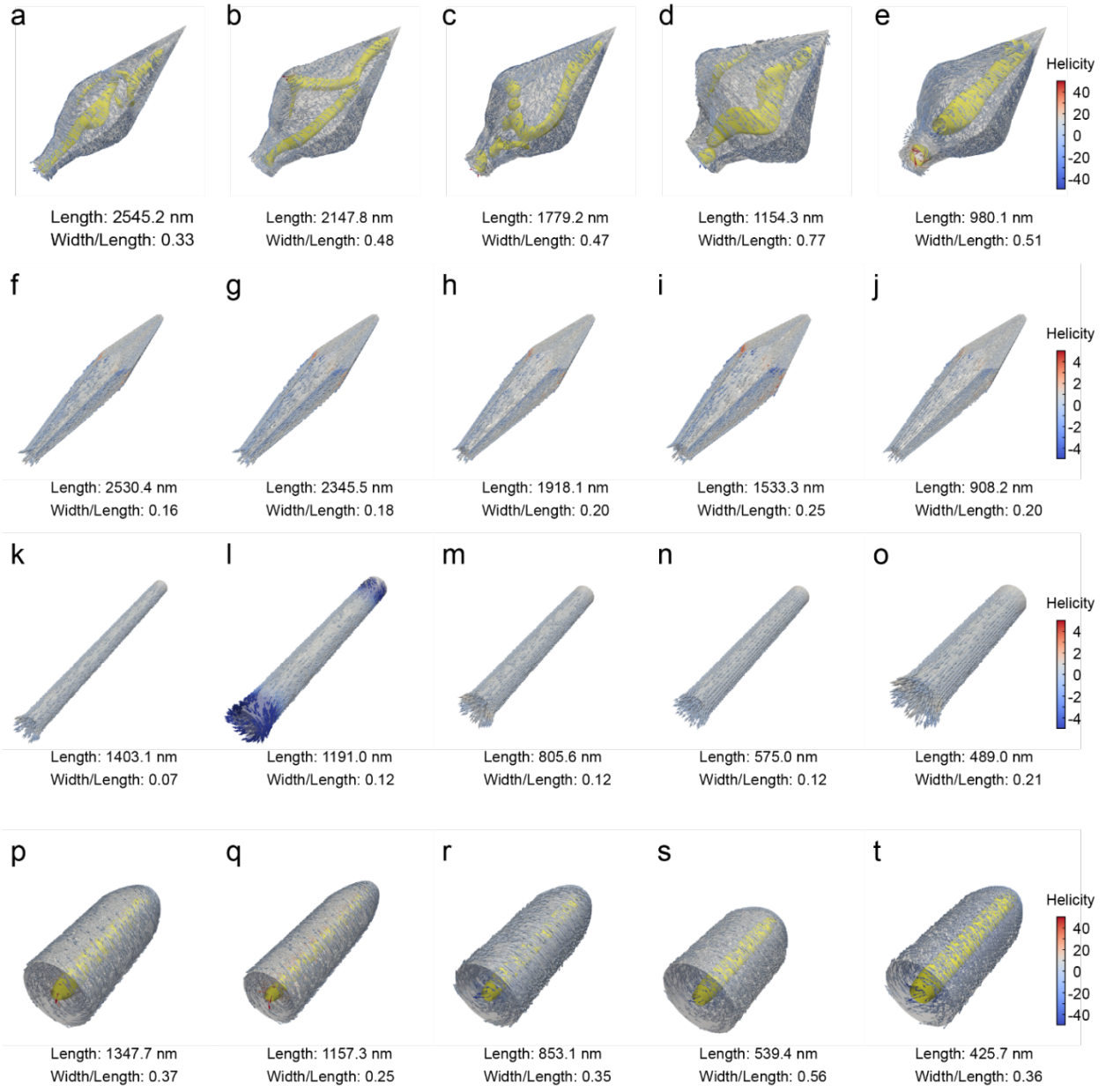

Fig. 8. Micromagnetic simulations of magnetic domain states for typical observed giant magnetite crystals of variable morphologies and sizes. The domain structures of saturated isothermal remanent magnetization are calculated along the axis parallel to the crystal elongation direction. (a-e) MD structure of all spearheads. (f-j) SD structure of all spindles. (k-o) SD structure of all needles. A needle of 1191 nm length with a width/length ratio of 0.12 shows a vortex structure at the ends of the particle (l). (p-t) Single vortex domain structure of all giant bullets. The crystal length and width/length ratio of each particle are indicated. Arrows showing magnetic moments were colored by helicity. Yellow surfaces show vortex cores.

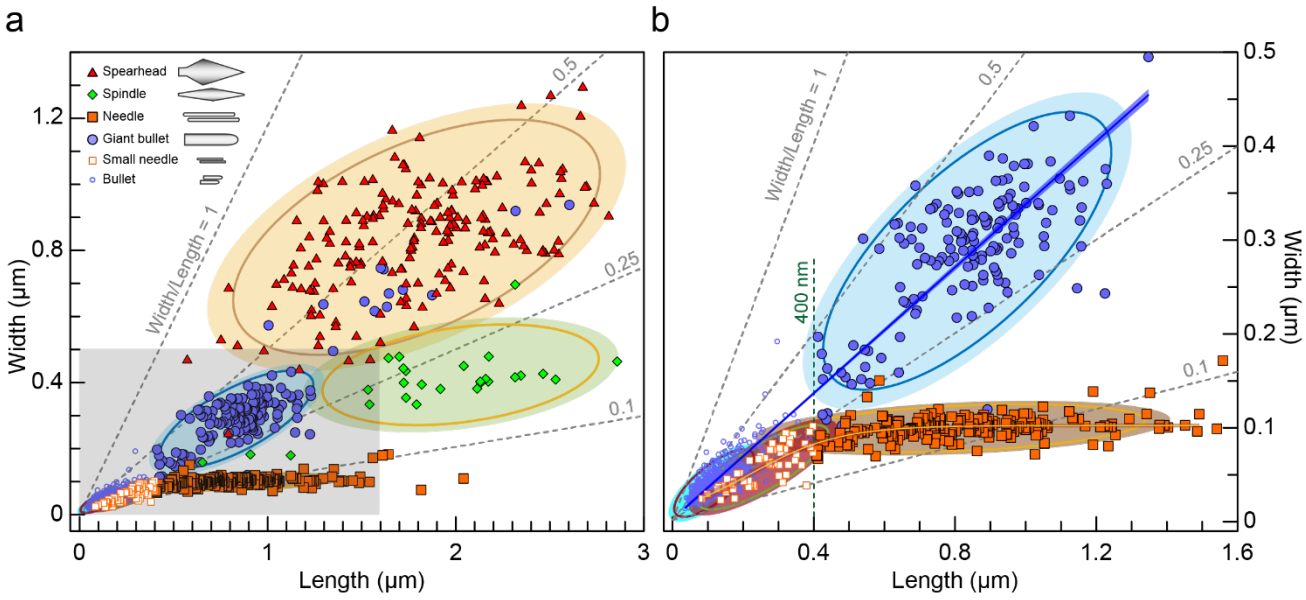

Fig. 9. Dimensional and morphological data analysis for magnetofossils in samples from Sites U1409 and U1403. (a) Plot of length versus width with calculated confidence ellipse for all types of giant magnetofossils, small needles, and bullets. Data for large dispersion degree were removed when calculating confidence ellipse: length for spearheads >3000 nm, width for spearheads >1500 nm; length for spindles <1500 nm; length for giant bullets >1500 nm, width for giant bullets >500 nm; length for needles >1500 nm. Coloured shadows indicate the 95% level of confidence ellipse, and inner solid lines correspond to the 90% level of confidence ellipse. (b) The enlarged grey area in (a). The solid yellow curve is a fit of the sigmoid function for small needles and needles: $W = a\ (1 + \exp(-k \times (L - b)))^{-1}$, where $a = 102.51 \pm 1.01$, $b = 222.03 \pm 8.33$, $k = (7.99 \pm 0.638) \times 10^{-3}$, $R^2 = 0.76$ (W and L are width and length). The solid blue curve is a fit of a linear function for bullets and giant bullets: $W = 0.34 \times L + 2.93$, $R^2 = 0.94$. The surrounding area correspond to the 95% confidence level.

607 Table 1. Samples from Exp. 342 that were subjected to electron microscopic analyses.

IODP Hole	Section	Interval (cm)	Depth (mbsf)	Depth (mcd)	Microscope analyses	Age* (ky +/- PEB)
U1409A	20X3W	20-21	154.00	179.67	SEM	144.65
U1409A	20X3W	30-31	154.10	179.77	TEM	135.65
U1409A	20X3W	56-57	154.36	180.03	SEM	112.25
U1409A	20X3W	65-66	154.45	180.12	SEM, TEM	12.00
U1409A	20X3W	93-94	154.73	180.40	TEM	-50.49
U1409A	20X3W	114-115	154.94	180.61	SEM	-91.26
U1409A	20X3W	127-128	155.07	180.74	SEM	-116.50
U1409C	21X2W	24-25	159.04	178.09	SEM	-
U1409C	21X3W	7-8	160.14	179.19	SEM	-
U1409C	21X3W	25-26	160.32	179.37	SEM	-
U1409C	21X3W	39-40	160.46	179.51	SEM	-
U1403B	22H1W	40-41	173.40	196.94	SEM	328.67
U1403B	23X1W	14-15	176.04	200.70	SEM	55.53
U1403B	23X1W	44-45	176.34	201.00	SEM	33.89
U1403B	23X1W	135-136	177.25	201.91	SEM	-141.94
U1403B	23X3W	55-56	179.05	203.71	SEM	-722.58
U1403A	28XCC	10-11	242.11	270.90	SEM	Note

608 Original *age is obtained from Penman et al. (2016). Note: the absolute age for this sample is ~70 Ma,
609 which is obtained from Norris et al. (2012). PEB, Palaeocene-Eocene boundary; +/- PEB indicates
610 before (-) and after (+) the PEB.